

## **Supplementary Information:**

Materials and Methods

Figures S1-S7

Tables S1-S3

References (1-41)

## **Supplementary Information for**

### **Solar fuels photoanode materials discovery by integrating high-throughput theory and experiment**

**Authors:** Qimin Yan<sup>1,2\*</sup>, Jie Yu<sup>3,4,5</sup>, Santosh K. Suram<sup>3</sup>, Lan Zhou<sup>3</sup>, Aniketa Shinde<sup>3</sup>, Paul F. Newhouse<sup>3</sup>, Wei Chen<sup>4</sup>, Guo Li<sup>1,2,5</sup>, Kristin A. Persson<sup>4,6</sup>, John M. Gregoire<sup>3\*</sup>, Jeffrey B. Neaton<sup>1,2,7\*</sup>

#### **Affiliations:**

<sup>1</sup> Molecular Foundry, Lawrence Berkeley National Laboratory, Berkeley, California 94720, United States

<sup>2</sup> Department of Physics, University of California, Berkeley, CA 94720, United States

<sup>3</sup> Joint Center for Artificial Photosynthesis, California Institute of Technology, Pasadena, CA 91125, United States

<sup>4</sup> Environmental Energy Technologies Division, Lawrence Berkeley National Laboratory, Berkeley, CA 94720, United States

<sup>5</sup> Joint Center for Artificial Photosynthesis, Lawrence Berkeley National Laboratory, Berkeley, CA 94720, United States

<sup>6</sup> Department of Materials Science and Engineering, University of California, Berkeley, California 94720, United States

<sup>7</sup> Kavli Energy NanoSciences Institute at Berkeley, Berkeley, CA 94720, United States

\*Correspondence to: qiminyan@temple.edu, gregoire@caltech.edu, jbneaton@lbl.gov

## Literature phases and screening criteria

Our literature survey to identify previously-reported phases was aimed at identifying metal oxide compounds that meet the following criteria:

1. Measured band gap (direct or indirect) in the range 1.2-2.8 eV
2. Photoelectrocatalytic (PEC) experiment demonstrating anodic photocurrent in an aqueous electrolyte (regardless of the pH) without the addition of a sacrificial reagent

These criteria are commensurate with those of the screening pipeline, which is reflected in the high throughput screening results. All 4 previously-reported photoanodes in the search space (pure VO<sub>4</sub> motif phases in Supplementary Table 1) passed all computational screening criteria and the 3 of those phases that were experimentally synthesized passed the remainder of the experimental screening criteria. Supplementary Table 1 includes 6 metal vanadates that contain V-O structures beyond that of the present focus (VO<sub>4</sub> in d<sup>0</sup> configuration), and it is worth noting that the set of cations in these phases (Fe, Cu, Ni, Bi) is a subset of the cations that appear in the pipeline-identified phases, indicating that the VO<sub>4</sub>-scaffold hypothesis may be generalized to include structures with a partial VO<sub>4</sub> motif and motivating further research to this effect.

Concerning the maximum solar water splitting efficiencies attainable with these metal oxide photoanodes, we consider the model recently presented by Fountaine et al. (1) that provides “realistic limiting efficiencies.” For their “Earth abundant photodiodes” device, the global maximum efficiency is 16.2% and the lowering of the photoanode band gap from 2.4 eV to 1.8 eV provides an approximately 2-fold increase in device efficiency. For their “high performance” device the global maximum efficiency is 28.3% and the lowering of the photoanode band gap from 2.4 eV to 1.8 eV increases the limiting device efficiency from approximately 7.3% to 22%, a 3-fold increase.

Table S1: The 16 previously-reported photoanode phases noted in the manuscript along with the reference demonstrating photoelectrocatalytic activity.

phase	Band gap (eV)	Pure VO <sub>4</sub> motif	Ref.
Fe <sub>2</sub> WO <sub>6</sub>	1.5		(2)
α-Fe <sub>2</sub> O <sub>3</sub>	1.9		(3)
Fe <sub>2</sub> VO <sub>4</sub>	1.9		(4)
FeV <sub>2</sub> O <sub>4</sub>	1.9		(4)
FeVO <sub>4</sub>	1.9	Y	(4-6)
ZnFe <sub>2</sub> O <sub>4</sub>	1.923		(7, 8)
α-CuV <sub>2</sub> O <sub>6</sub>	1.95		(9)
β-Cu <sub>3</sub> V <sub>2</sub> O <sub>8</sub>	2.05	Y	(10)
BiFeO <sub>3</sub>	2.1		(11)
Bi <sub>4</sub> V <sub>2</sub> O <sub>11</sub>	2.15		(12)
NiV <sub>2</sub> O <sub>6</sub>	2.16		(13)
Fe <sub>2</sub> TiO <sub>5</sub>	2.2		(14)
α-Ag <sub>3</sub> VO <sub>4</sub>	2.2	Y	(15)
Fe <sub>2</sub> V <sub>4</sub> O <sub>13</sub>	2.25		(16)

CuWO <sub>4</sub>	2.34		(17)
BiVO <sub>4</sub>	2.4	Y	(18)

### Choice of computational method for band gaps

The focus of this work is to identify new ternary oxides that exhibit efficient optoelectronic function including band gaps and band edges. Given the number of ternary oxides and their chemical complexity, a high-throughput survey is a challenging task, and an exhaustive search through the whole of material space is not feasible. We require a well-defined search space and a screening pipeline with multiple layers. DFT is the formalism of choice for estimating properties related to optoelectronic functionality. However, static DFT is a ground-state theory; and although Kohn-Sham orbital energies generate an approximate band structure and spectrum, standard semilocal functionals underestimate the band gaps of semiconductors and lead to (sometimes considerable) band gap and self-interaction errors, the latter a particular challenge for localized d-states in TMOs (19), such as those of interest here. DFT+U reduces self-interaction errors for localized states by including an on-site repulsion on transition metal d electrons, but there are still limitations associated with the use of DFT for band gaps and optical properties. To overcome the well-known band-gap underestimation problem induced by local or semi-local DFT methods, different levels of electronic structure theory have been proposed for the high-throughput computational screening of band gaps, including  $\Delta$ -sol (19), GLLB-SC (20), and ab initio many-body perturbation theory within the GW approximation and the Bethe-Salpeter equation (BSE) approach (21, 22). The so-called ab initio GW-BSE method is currently the formalism of choice for accurate band structures and optical properties. A rigorous excited-state method, GW-BSE can provide accurate band gaps and optical spectra for disperate classes of materials. However, the computational cost of GW-BSE is significantly greater than DFT; and moreover, such calculations rely on a careful choice of starting point and are rather sensitive to convergence (23); and therefore GW-BSE calculations for a large number of materials are not feasible for this study. Previous studies (19, 24) have shown that DFT spectra obtained with the HSE functional – a hybrid functional featuring local fractional exact exchange – can be approximately predictive for band gaps for a range of materials. DFT-HSE has also been proven to be an accurate tool to explore the fundamental chemistry and physics of strongly correlated oxides (24). In this study, we use DFT with the HSE functional and a modified mixing parameter ( $\alpha=0.17$ ) as a compromise between accuracy and efficiency. In screening for band gaps across 121 compounds, we neglect exchange and correlation effects absent in DFT-HSE generalized Kohn-Sham single-particle spectra; and we neglect electron-hole interactions. Additionally, here we evaluate direct and indirect gaps as differences in DFT-HSE generalized Kohn-Sham eigenvalues, fully considering the materials space independent of whether lowest-energy transitions are symmetry-allowed or symmetry-disallowed.

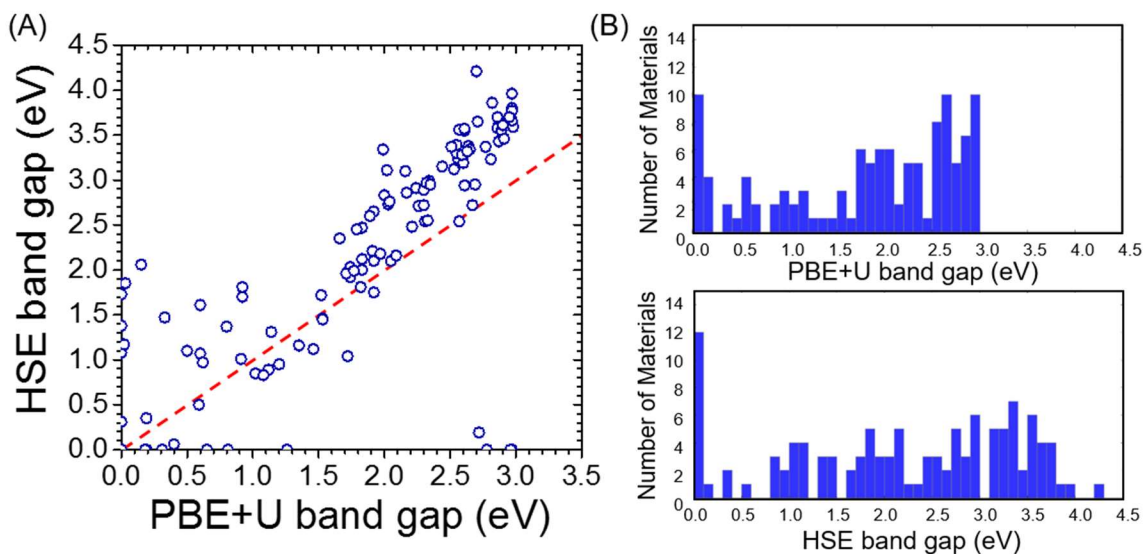


Figure S1. (A) Calculated band gaps with both HSE( $\alpha=0.17$ ) and PBE+U for 116 ternary metal vanadates with PBE+U band gaps below 3.0 eV. (B) The distribution of band gaps for both HSE and PBE+U methods. The plot data are included in the SI Appendix, Table S3.

#### Details of high-throughput computations

All the high-throughput DFT computations are performed using the Vienna software package (VASP) (25),(26) with the PAW pseudopotentials (27), the generalized gradient approximation (GGA) as implemented by Perdew, Burke and Ernzerhoff (PBE) (28), and the screened hybrid functional of Heyd, Scuseria, and Ernzerhof (HSE) (29, 30). The mixing parameter for the Hartree-Fock exchange potential is reduced from 25% to 17%, based on the success of the latter value for predicting gaps of known metal vanadates (including  $\text{BiVO}_4$  and  $\text{CuO-V}_2\text{O}_5$  systems). We refer to this functional as HSE( $\alpha=0.17$ ). A uniform reduction factor for the q-point grid representation of the exact exchange potential ( $\text{NKRED} = 2$ ) is applied to accelerate the HSE calculations. An even-number Gamma-centered k-point mesh for the integrations over the Brillouin zone is used with k-point densities at or larger than 1000 k-points per atom (kppa). Spin-polarization is included in all calculations. The lattice parameters employed in this work are obtained from the Materials Project database which are calculated using the PBE+U functional with the high-throughput computation parameters described by Jain *et al.* (31). The Hubbard U values used in the PBE+U calculations are adopted from the previous work (32). We use an energy cutoff of 400 eV for the static HSE( $\alpha=0.17$ ) calculations and surface slab calculations. All data analysis is performed using the Pymatgen package (33).

#### Band gap energies

DFT-HSE (with a mixing parameter of  $\alpha=0.17$ , modified from the standard value of 0.25) and DFT-PBE+U band gaps for the 116 metal vanadates are shown in Supplementary Fig. 1a. It is clear that the correlation between the HSE( $\alpha=0.17$ ) and PBE+U band gaps is not simple enough to be described by a “scissor” shift, motivating the use of HSE( $\alpha=0.17$ ) in this study. This fact is also manifested by the different energy distribution of band gaps obtained by PBE+U and HSE( $\alpha=0.17$ ) [Supplementary Fig. 1b]. Note that the band gap difference is dependent on the choice of Hubbard U in PBE+U or the choice of screening parameter in HSE. The discrepancy

between HSE and PBE+U results becomes especially large for the band gaps that are relevant to photocatalysis. For oxides with a HSE( $\alpha=0.17$ ) band gap between 1.2 eV and 2.8 eV, its PBE+U band gap is within a range between 0 eV and 2.5 eV. It indicates that our choice of the PBE+U band gap window ( $< 3$  eV) for the first screen layer is appropriately restrictive to avoid false-negative results that would erroneously exclude a promising phase for experimental study.

### Band edge energies relative to vacuum

In order to predict the absolute positions of band edge energies, several methods based on different assumptions have been employed in the literature. For example, an empirical method based on atomic Mulliken electro-negativities from bulk calculations has been used to predict the band edge positions (34, 35). However, as pointed out in Ref. (36), this method can lead to errors for some transition metal oxides of more than 1 eV. Also, this approach is not able to correctly predict the difference in band edge positions for materials with the same formula unit but different crystal symmetries. For instance, rutile and anatase  $\text{TiO}_2$  are known to have similar band gaps, while the band offset between these two phases is as large as 0.4 eV (37).

Previous work shows that a reliable prediction of the position of the semiconductor band edges relative to the two reaction potentials in the presence of aqueous solution can be realized via the knowledge of the band edge energies relative to the vacuum (36). Band edge energies with respect to vacuum can provide a good estimate of the alignment of the semiconductor band edges with water redox potential without computationally-demanding explicit calculations of semiconductor/water interfaces. Also, it has been shown that the lowest energy surface orientations and terminations are the most relevant for predicting band edge energies (36). It indicates that in complex systems without enough experimental information the search for the lowest energy surface orientation and/or termination becomes essential.

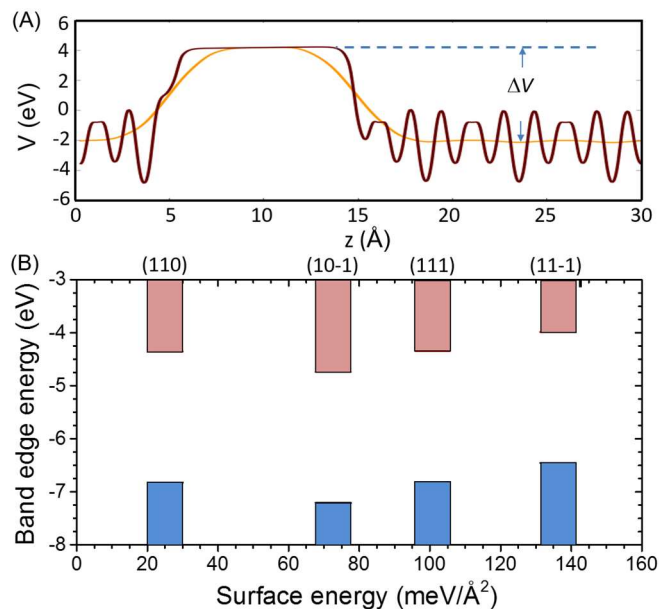


Figure S2. (A) The averaged electrostatic potential (in black) and macroscopic electrostatic potential (in green) of a sample surface slab system. (B) The band edge energies for mon-CrVO<sub>4</sub> with different surface orientations.

In this work, we employ a standard two-step scheme to calculate the band edge energies relative to the vacuum level. In the bulk the electronic eigenvalues are referenced to the average electrostatic potential (ionic and Hartree). From calculations of a supercell with a surface slab region and a vacuum region, the vacuum level can be defined by the potential far away from the surface slab, well in the vacuum region; the macroscopically averaged electrostatic potential taken from deep inside the slab is defined as the “bulk” average electrostatic potential. In this manner, the potential step  $\Delta V$  between the vacuum and the bulk is established and the bulk electronic eigenvalues can be referenced to the vacuum. As an example, the average electrostatic potential of the  $(001)$  surface slab of a candidate oxide is shown in Supplementary Fig. 2a. Note that  $\Delta V$  is surface orientation and termination dependent.

Recently, combining the quasiparticle perturbation theory GW and DFT (+U) methods, this methodology has been used for calculating the absolute band edge positions of 14 transition metal oxides and obtained a reasonably good agreement with experiment(36). The rationale behind this choice is that the potential distribution in the slab model depends primarily on the charge density which is the ground state quantity and hence could be relatively well described by the traditional DFT(+U) method. In this work, we evaluate the absolute band edge positions by combining DFT-HSE( $\alpha=0.17$ ) bulk calculations and PBE+U surface slab calculations. This combination has been used to evaluate the band alignment in traditional nitride semiconductors (38) and good agreement with experiment have been achieved. Supplementary Figure 2b shows the absolute band edge energies of mon-CrVO<sub>4</sub> for several different surface orientations with different surface energies. Clearly, the band edge energies are sensitive to surface orientations/terminations. This observation is consistent with the previous work(36) and reveals the need for explicit calculations of band edge positions for different surface orientations.

The surface slabs are constructed using an automated workflow developed in a previous work (39). We only consider low Miller index  $(h, k, l)$  [smaller than  $(111)$ ] and non-polar surfaces as those surfaces are typically of lowest energy and likely not to reconstruct. Different terminations are considered for each specific surface orientation. We generate around 600 surface slab systems for 43 metal vanadates, carry out structural relaxations, and compute the surface energies which are defined as the total energy difference between the slab and the bulk systems per unit of surface area:  $E_s = \frac{E_{slab} - E_{bulk}}{2A}$ , where  $A$  is the surface area,  $E_{slab}$  is the total energy of slab, and  $E_{bulk}$  is the total energy of bulk with equivalent number of atoms. We compute band edge energies from surfaces with lowest surface energies. Since the  $E_{VBM}$  screening criterion (tier 4) is particularly lenient, we note that the down-selection of phases in the pipeline is somewhat insensitive to the approximation of  $E_{VBM}$  using the lowest-energy surface since the higher energy surfaces also typically pass the screening criterion. This approximation is most pertinent for the results of Fig. 3 where the  $E_{VBM}$  exhibits strong anti-correlation with the valence band character parameter, and we note that this general trend is also robust to the selection of band edge energy among the low index surfaces.

### Crystal structures and comparison with experiment

To avoid expensive structural relaxations with the HSE functional, the structures under investigation are obtained from the Materials Project database relaxed with PBE+U. To validate this choice, we perform the structural relaxation with both HSE and PBE+U for 41 transition metal oxides in the ICSD database. The comparisons for the calculated equilibrium volume with experimental data are shown in Supplementary Fig. 3.

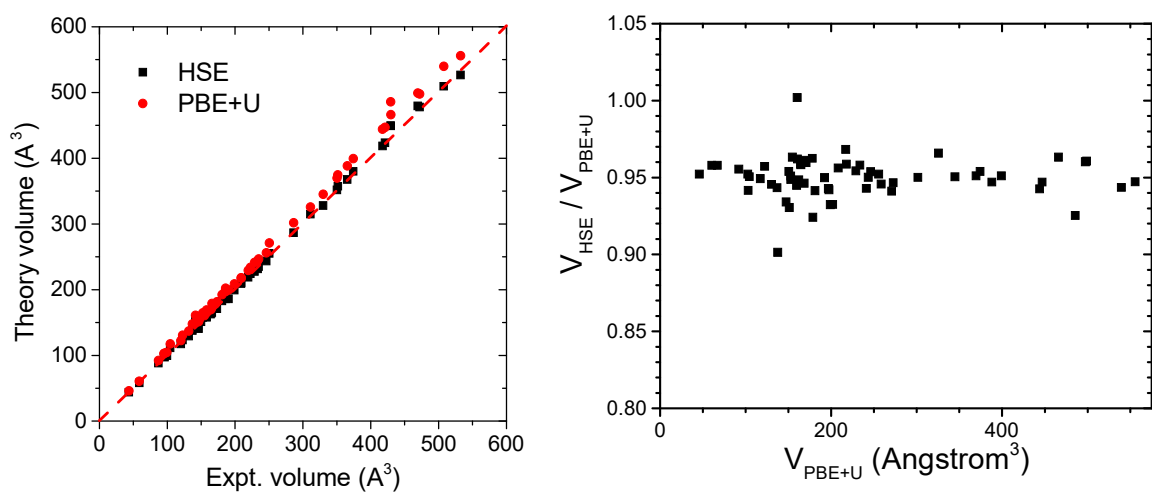


Figure S3 (A) Comparison between the calculated equilibrium volumes for 41 transition metal oxides obtained from both HSE( $\alpha=0.25$ ) and PBE+U methods and the experimental data obtained from the ICSD database. (B) The volume ratio between the equilibrium lattice structures relaxed with PBE+U and these relaxed with HSE( $\alpha=0.25$ ).

Clearly, the equilibrium volume data obtained using HSE achieve an excellent agreement with experimental data with a mean error of 0.2% difference. On the other hand, as expected, PBE+U tends to overestimate the equilibrium volume of materials. In spite of that, the differences in the unit cell volume between PBE+U and HSE are within a reasonable range between 3% and 8% (Supplementary Fig. 3b). The HSE band gaps calculated at PBE+U structures are in general only slightly smaller than those obtained at HSE structures with an average difference of less than 0.2 eV. Given the fact that the changes in lattice parameters and band gaps scale almost linearly with the change in mixing parameter, we expect that the difference between PBE and HSE( $\alpha=0.17$ ) should be smaller than that between PBE and HSE( $\alpha=0.25$ ). We thus conclude that it is feasible to perform the HSE( $\alpha=0.17$ ) electronic structure calculations using the PBE+U relaxed structures without introducing additional significant errors in the estimated band gaps.

### Magnetic ordering

Although all PBE+U calculations in the MP database are spin-polarized, only ferromagnetic (FM) spin configurations are considered. In transition metal oxides, the exchange interaction can be strong enough to make the antiferromagnetic (AF) configurations more favorable even at room temperature. For instance, NiO, MnO, and Fe<sub>2</sub>O<sub>3</sub> are known to be stable in AF spin ground states at room temperature.

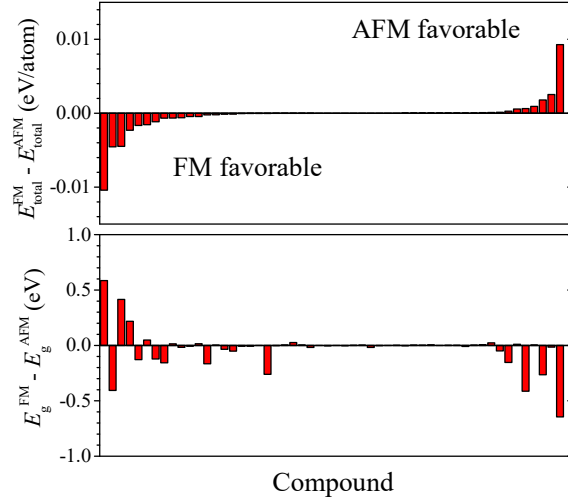


Figure S4. (A) Differences in the total energies per atom between the FM phases and AFM/FR phases for 55 transition metal oxides. (B) Differences in the band gaps between the FM and AFM/FR phases for 55 transition metal oxides.

To validate our choice, we study the energetics and electronic structures of some selected transition metal oxides in three simple magnetic structures including FM, AF, and ferrimagnetic (FR) spin configurations. We develop an automatic scheme to generate the initial antiferromagnetic magnetic orderings. Firstly, we create the supercells which are automatically expanded from the primitive unit cells and contain at least 8 atoms for each magnetic elements. We then treat the spin up and spin down species for the same element as two different elements, and choose the AF spin configuration with highest symmetries (largest space group numbers) as an initial guess of the stable AF (or FR) configurations. The initial magnetic moment on each magnetic atom is set to be the highest possible value according to the number of occupied d-electrons.

With the relaxation of both the structural and the magnetic degree of freedom using the PBE+U method, we obtain the total energies and the band gaps of these magnetic phases. As shown in Supplementary Fig. 4a, FM phases are more energetically favorable for most of the selected transition metal oxides. Furthermore, as shown in Supplementary Fig. 4b, the difference in band gaps between the two magnetic configurations is smaller than 0.2 eV for most compounds. We therefore choose FM phase as the default magnetic configuration in our data-driven high-throughput computational screening process.

#### Definition of band characters at band edges

The band character of V 3d at the CBM is defined as  $W_{V,3d} = \int_{E_{CBM}}^{E_{CBM}+0.5 \text{ eV}} \frac{DOS(V,3d)}{DOS(total)} dE$ , where  $E_{CBM}$  is the energy of the CBM,  $DOS(total)$  is the total density of states, and  $DOS(V,3d)$  is the projected density of states for V 3d orbitals. The band character of O 2p at the VBM is defined as  $W_{O,2p} = \int_{E_{VBM}-0.5 \text{ eV}}^{E_{VBM}} \frac{DOS(O,2p)}{DOS(total)} dE$ , where  $E_{VBM}$  is the energy of the VBM and  $DOS(O,2p)$  is the projected density of states for O 2p orbitals.

A summary of the computational screening results is provided in Supplementary Table 3.

## PVD and XRD experiments

The metal-vanadium (M-V) oxide composition libraries were fabricated using RF magnetron co-sputtering onto 100 mm-diameter, 2.2 mm-thick glass substrates with a Fluorine doped Tin oxide (FTO) coating (Tec7, Hartford Glass Company) in a sputter deposition system (Kurt J. Lesker, CMS24) with  $10^{-5}$  Pa base pressure. Co-sputtering was performed using a V target and an additional metal target (M) with the exception of the Ag-containing libraries, which used an  $\text{Ag}_2\text{O}$  target. The composition libraries were either deposited as “metal” or “oxide” thin films, referring to the absence or presence of reactive  $\text{O}_2$  in the chamber. The working atmosphere was composed of inert sputtering gas Ar (0.72 Pa) and reactive gas  $\text{O}_2$  (0.08 Pa) for oxide depositions, and 0.80 Pa Ar for metal deposition. The composition gradients in the co-sputtered continuous composition spreads were attained by positioning the deposition sources in a non-confocal geometry. The power applied on each source was adjusted according to the deposition rate calibration from the sputter source. The film thickness was not measured for each composition library but was estimated to be 200 nm based on the deposition rate calibration assuming the average molar density of the elemental oxides. The as-deposited composition libraries were subsequently placed flat on a quartz support and annealed in a Thermo Scientific box oven in flowing air at various temperatures and durations. The annealing was preceded by a 2 h temperature ramp and was followed by free-cooling to near ambient temperature. Supplementary Table 2 summarizes the deposition and annealing conditions for the 15 phases identified by the screening pipeline.

The crystal structures and phase distribution of the composition libraries were determined through XRD measurements using a Bruker DISCOVER D8 diffractometer with  $\text{Cu K}_\alpha$  radiation from a Bruker  $\text{I}\mu\text{S}$  source. The x-ray spot size was limited to a 1 mm length scale, over which the composition is constant to within approximately 1%. The XRD measurements were performed on a series of evenly-spaced positions along the composition gradient. Diffraction images were collected using a two-dimensional VÅNTEC-500 detector and integrated into one-dimensional patterns using DIFFRAC.SUITE™ EVA software. For patterns in which multiple crystalline phases were identified, the relative phase fraction of each phase was calculated using the measured intensity and relative sensitivity factor of the most distinguishing peak of each phase. Partial XRD patterns for representative phases are shown in Supplementary Figure 5 to illustrate phase identification.

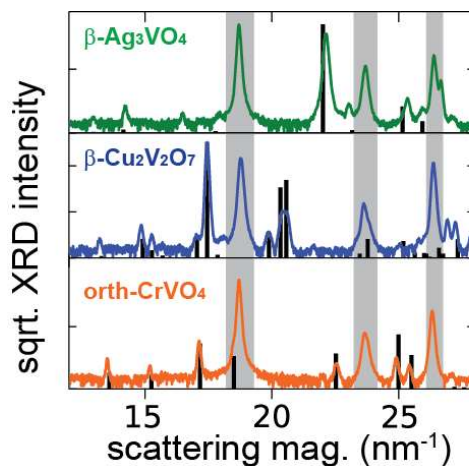


Figure S5: Partial XRD patterns for 3 representative phases where the reference patterns are shown as black lines and regions with strong substrate signal are noted with gray boxes.

Table S2: The deposition and annealing conditions are listed for the 15 phases identified by the screening pipeline along with Materials Project identification numbers (mp-id). All the vanadate

depositions used metal targets (M and V), except a silver oxide (Ag<sub>2</sub>O) target was used for the Ag-V libraries.

mp-id	Phase	Deposition condition			Annealing condition	
		Metal or oxide deposition	V power (W)	M power (W)	temperature (°C)	Duration (hrs)
<a href="#">mp-851269</a>	Cr <sub>2</sub> V <sub>4</sub> O <sub>13</sub>	metal	150	70	610	1
<a href="#">mp-19418</a>	orth-CrVO <sub>4</sub>	metal	150	70	610	1
<a href="#">mp-19688</a>	mon-CrVO <sub>4</sub>	oxide	150	165	550	3
<a href="#">mp-540630</a>	tri-FeVO <sub>4</sub>	metal	150	43.5	610	1
<a href="#">mp-773310</a>	α-CoV <sub>2</sub> O <sub>6</sub>	oxide	160	55	550	3
<a href="#">mp-540833</a>	Co <sub>3</sub> V <sub>2</sub> O <sub>8</sub>	oxide	160	55	550	3
<a href="#">mp-557404</a>	Ni <sub>2</sub> V <sub>2</sub> O <sub>7</sub>	oxide	150	52	550	3
<a href="#">mp-542151</a>	Ni <sub>3</sub> V <sub>2</sub> O <sub>8</sub>	oxide	150	52	550	3
<a href="#">mp-505508</a>	α-Cu <sub>2</sub> V <sub>2</sub> O <sub>7</sub>	oxide	150	6	610	1
<a href="#">mp-559660</a>	β-Cu <sub>2</sub> V <sub>2</sub> O <sub>7</sub>	oxide	150	11	550	10
<a href="#">mp-540833</a>	γ-Cu <sub>3</sub> V <sub>2</sub> O <sub>8</sub>	oxide	150	6	610	1
<a href="#">mp-505456</a>	Cu <sub>11</sub> V <sub>6</sub> O <sub>26</sub>	oxide	150	6	610	1
<a href="#">mp-18889</a>	α-Ag <sub>3</sub> VO <sub>4</sub>	oxide	150	Ag <sub>2</sub> O, 47	550	3
<a href="#">mp-19412</a>	β-Ag <sub>3</sub> VO <sub>4</sub>	oxide	180	Ag <sub>2</sub> O, 30	300	10
<a href="#">mp-504878</a>	mon-BiVO <sub>4</sub>	oxide	175	14	550	3

For each M-V system, multiple composition libraries were typically synthesized using both metal and oxide depositions and different annealing conditions. In instances where multiple synthesis conditions yielded the same target phase in sufficiently high purity to pass tier 5 criteria, all such libraries were passed to tier 6 and 7 screening, and the sample exhibiting the cleanest UV-vis and PEC data was chosen to represent the target phase. In total, ~50 M-V oxide libraries were synthesized in tier 5 screening, highlighting the need for high throughput experiments to sufficiently evaluate computational predictions.

### UV-vis experiments

Ultraviolet-visible (UV-vis) absorption spectroscopy was performed using a custom scanning spectroscopy instrument described in detail previously.<sup>(40)</sup> Briefly, the dual integrating sphere system measured both the fractional transmittance (T) and reflectance (R) at 1521 locations across the entire 100 mm substrate (sample pitch = 2 mm) using illumination from a 200 W (Hg)Xe broadband source (Newport/Oriel Apex) and Spectral Products, Inc. model SM303 spectrometers. The T and R signals were used to calculate the spectral absorption coefficient ( $\alpha$ ) up to a factor of film thickness ( $\tau$ ):  $\alpha \times \tau = -\ln[T \times (1-R)^{-1}]$  from which direct and indirect Tauc plots were generated. Band gap energies were estimated from the Tauc plots using a constrained piece-wise linear fitting based algorithm. While a direct band gap energy was obtained from each direct-allowed Tauc signal, several indirect-allowed Tauc signals did not exhibit a clear transition, resulting in the use of an inequality expressing the upper limit of the indirect band gap energy. Representative Tauc signals and band gap extractions are shown in Supplementary Fig. 6. Typically each target phase existed over a sufficiently large area of the film that dozens of UV-vis spectra were acquired on samples with high phase purity, and the reported band gap values were validated through manual inspection of many corresponding Tauc spectra.

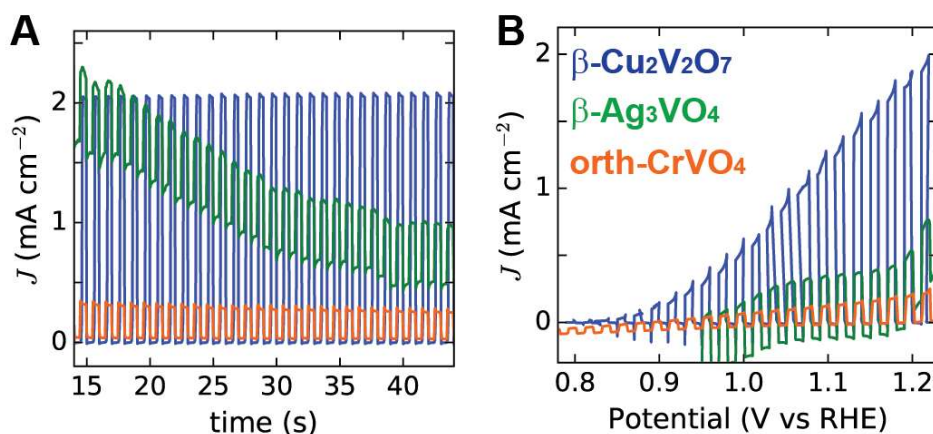


Figure S7: Toggled-illumination chronoamperometry (A, 1.23 V vs RHE) and linear sweep voltammetry (B, -0.02 V s<sup>-1</sup>) in pH 9.2 electrolyte. Of these 3 phases, orth-CrVO<sub>4</sub> exhibits the highest photovoltage but lowest photocurrent,  $\beta$ -Ag<sub>3</sub>VO<sub>4</sub> exhibits a varying dark current signal (believed to be from a minority phase) that does not strongly impact the photoactivity, and  $\beta$ -Cu<sub>2</sub>V<sub>2</sub>O<sub>7</sub> exhibits high, stable photocurrent.

### PEC experiments

A scanning drop electrochemical cell (SDC) was utilized to perform photoelectrochemical (PEC) experiments on the PVD libraries as described in our previous work.<sup>(41)</sup> An aqueous electrolyte made up of 0.1 M boric acid, 0.05 M potassium hydroxide, and 0.25 M sodium sulfate (pH 9) provided continuous flow into the 3-electrode cell while a 385 nm light emitting diode (LED, Thor Labs, M385F1, 0.7 A current limit, 3 mW illumination power) provided illumination. Short circuit photocurrent density (0 V vs. O<sub>2</sub>/H<sub>2</sub>O Nernstian potential; 1.23 V vs. RHE) was calculated from toggled-illumination (0.5 s on, 0.5 s off) chronoamperometry (CA) measurements over 44 s, a portion of which is shown in Supplementary Figure 7 for three representative samples. The average current from a portion of the illuminated period was subtracted by the average current from a portion of the previous dark period and divided by the circular illumination area (1.5 mm diameter) to provide values for  $J_{O_2/H_2O}$  in Table 1 and Figure 2. All 16 phases in tier 6, Figure 1, were measured for PEC activity, 15 of which resulted in measurable photocurrent. Linear sweep voltammetry (LSV) starting at 1.23 V vs RHE was performed on each sample after the CA measurement, and while the LSV data was not used to generate screening criteria, manual inspection of the LSV was performed to confirm the photoactivity of each phase. For example, the CA characterization of  $\beta$ -Ag<sub>3</sub>VO<sub>4</sub> reveals a substantial dark current indicating the presence of a non-PEC reaction. Inspection of both the CA and LSV reveal that the photocurrent remains nearly constant despite strong variation in the dark current. This example includes the lowest-purity phase to pass tier 5 screening, for which the thin film samples contains fcc-Ag as a minority phase. Correspondingly, the anodic dark current in the CA is likely due to electrooxidation of Ag, and the onset of cathodic dark current in the LSV due to its electroreduction, both of which proceed without impacting the photoactivity of  $\beta$ -Ag<sub>3</sub>VO<sub>4</sub>. While Faradaic efficiency measurements are not available in the high throughput PEC experiments, this type of detailed analysis is applied to each tier-7 phase to confirm that the observed photoactivity is due to OER photoelectrocatalysis by the majority phase. While PEC stability is a primary focus of ongoing work, we note that for photoactive phases for which the photocurrent is primarily due to photoanodic corrosion, the photocurrent typically vanishes over

the 44 s CA measurement, prompting our use of the photocurrent at the end of the 44 s CA as the screening criterion.

Table S3. Materials information for 174 tier 1 compounds including the farthest tier achieved by each phase.

Materials Project ID	Formula	E above Hull (eV/atom)	PBE+U band gap (eV)	Farthest tier	HSE indirect band gap (eV)	V 3d character at CBM	O 2p character at VBM	VBM energy (eV)
mp-18812	NdVO <sub>4</sub>	0.0000	3.02	Tier1				
mp-18734	HoVO <sub>4</sub>	0.0000	3.03	Tier1				
mp-19169	PrVO <sub>4</sub>	0.0000	3.03	Tier1				
mp-18815	KVO <sub>3</sub>	0.0000	3.04	Tier1				
mp-18827	AlVO <sub>4</sub>	0.0000	3.04	Tier1				
mp-25726	V <sub>2</sub> Pb <sub>3</sub> O <sub>8</sub>	0.0000	3.05	Tier1				
mp-19031	RbVO <sub>3</sub>	0.0000	3.05	Tier1				
mp-556791	K <sub>5</sub> V <sub>3</sub> O <sub>10</sub>	0.0000	3.06	Tier1				
mp-540778	CsVO <sub>3</sub>	0.0000	3.11	Tier1				
mp-19162	LaVO <sub>4</sub>	0.0000	3.12	Tier1				
mp-19083	NaVO <sub>3</sub>	0.0000	3.23	Tier1				
mp-19034	Mg <sub>3</sub> V <sub>2</sub> O <sub>8</sub>	0.0000	3.31	Tier1				
mp-565574	K <sub>4</sub> V <sub>2</sub> O <sub>7</sub>	0.0000	3.44	Tier1				
mp-19660	Sr <sub>2</sub> V <sub>2</sub> O <sub>7</sub>	0.0000	3.45	Tier1				
mp-19474	Ba <sub>2</sub> V <sub>2</sub> O <sub>7</sub>	0.0000	3.46	Tier1				
mp-19386	Sr <sub>3</sub> V <sub>2</sub> O <sub>8</sub>	0.0000	3.68	Tier1				
mp-19365	Ba <sub>3</sub> V <sub>2</sub> O <sub>8</sub>	0.0000	3.74	Tier1				
mp-780545	Na <sub>3</sub> VO <sub>4</sub>	0.0000	4.03	Tier1				
mp-19219	Li <sub>3</sub> VO <sub>4</sub>	0.0000	4.03	Tier1				
mp-639787	K <sub>3</sub> VO <sub>4</sub>	0.0000	4.04	Tier1				
mp-566195	Mg <sub>2</sub> V <sub>2</sub> O <sub>7</sub>	0.0013	3.16	Tier1				
mp-19368	Sr <sub>2</sub> V <sub>2</sub> O <sub>7</sub>	0.0014	3.39	Tier1				
mp-583094	Li <sub>3</sub> VO <sub>4</sub>	0.0028	3.94	Tier1				
mp-648893	Na <sub>4</sub> V <sub>2</sub> O <sub>7</sub>	0.0039	3.38	Tier1				
mp-542076	Ca <sub>3</sub> V <sub>2</sub> O <sub>8</sub>	0.0189	3.51	Tier1				
mp-764673	Na <sub>3</sub> VO <sub>4</sub>	0.0190	3.90	Tier1				
mp-19373	LiVO <sub>3</sub>	0.0201	3.03	Tier1				
mp-639402	K <sub>3</sub> VO <sub>4</sub>	0.0215	3.63	Tier1				
mp-25110	V <sub>2</sub> Pb <sub>3</sub> O <sub>8</sub>	0.0327	3.05	Tier1				
mp-18989	LaVO <sub>4</sub>	0.0357	3.51	Tier1				

mp-19052	K <sub>3</sub> VO <sub>4</sub>	0.0361	3.67	Tier1			
mp-763901	NaVO <sub>3</sub>	0.0425	3.21	Tier1			
mp-779358	Na <sub>3</sub> VO <sub>4</sub>	0.0477	4.02	Tier1			
mp-770094	Y <sub>2</sub> V <sub>2</sub> O <sub>7</sub>	0.0816	0.49	Tier1			
mp-771790	V <sub>3</sub> NiO <sub>8</sub>	0.0825	1.19	Tier1			
mp-761301	VIO <sub>4</sub>	0.0847	1.06	Tier1			
mp-510657	VCu <sub>3</sub> O <sub>4</sub>	0.0848	0.10	Tier1			
mp-783902	Dy <sub>2</sub> V <sub>2</sub> O <sub>7</sub>	0.0855	0.47	Tier1			
mp-779376	Na <sub>2</sub> V <sub>2</sub> O <sub>5</sub>	0.0872	0.97	Tier1			
mp-775570	Na <sub>3</sub> VO <sub>3</sub>	0.0881	0.22	Tier1			
mp-772127	V <sub>2</sub> CrO <sub>6</sub>	0.0898	0.00	Tier1			
mp-764595	Na <sub>2</sub> V <sub>2</sub> O <sub>5</sub>	0.0924	1.27	Tier1			
mp-772672	Sm <sub>2</sub> V <sub>2</sub> O <sub>7</sub>	0.0936	1.35	Tier1			
mp-853245	KV <sub>12</sub> O <sub>30</sub>	0.0937	0.37	Tier1			
mp-769865	VCr <sub>2</sub> O <sub>4</sub>	0.0938	0.08	Tier1			
mp-763248	V <sub>4</sub> FeO <sub>12</sub>	0.0953	0.01	Tier1			
mp-780306	Na <sub>2</sub> V <sub>2</sub> O <sub>5</sub>	0.0987	1.17	Tier1			
mp-32432	Mg <sub>2</sub> VO <sub>4</sub>	0.0989	0.00	Tier1			
mp-743557	V <sub>2</sub> Bi <sub>4</sub> O <sub>11</sub>	0.1009	2.50	Tier1			
mp-769665	VCoO <sub>4</sub>	0.1146	0.37	Tier1			
mp-649492	V <sub>2</sub> PbO <sub>6</sub>	0.1208	2.34	Tier1			
mp-771556	VCoO <sub>4</sub>	0.1413	0.26	Tier1			
mp-705670	V <sub>2</sub> Cu <sub>2</sub> O <sub>7</sub>	0.2036	0.00	Tier1			
mp-18740	V <sub>2</sub> Cd <sub>2</sub> O <sub>7</sub>	0.0000	2.56	Tier2	3.24	0.70	0.69
mp-18784	DyVO <sub>4</sub>	0.0000	2.98	Tier2	-	-	-
mp-18799	YbVO <sub>4</sub>	0.0022	0.00	Tier2	0.00	-	-
mp-18807	V <sub>2</sub> Zn <sub>2</sub> O <sub>7</sub>	0.0325	2.34	Tier2	2.99	0.71	0.66
mp-18880	ErVO <sub>4</sub>	0.0358	2.72	Tier2	0.19	0.03	0.72
mp-18929	BaV <sub>2</sub> O <sub>6</sub>	0.0000	2.86	Tier2	3.58	0.72	0.70
mp-18960	ErVO <sub>4</sub>	0.0000	2.97	Tier2	0.00	-	-
mp-18993	LuVO <sub>4</sub>	0.0000	2.94	Tier2	3.67	0.70	0.71
mp-19068	TmVO <sub>4</sub>	0.0000	2.96	Tier2	0.00	-	-
mp-19121	TbVO <sub>4</sub>	0.0000	2.98	Tier2	-	-	-
mp-19133	YVO <sub>4</sub>	0.0000	2.97	Tier2	3.80	0.68	0.72
mp-19142	Mn <sub>2</sub> V <sub>2</sub> O <sub>7</sub>	0.0000	1.20	Tier2	0.95	0.66	0.29
mp-19214	CeVO <sub>4</sub>	0.0485	0.00	Tier2	1.08	0.67	0.05
mp-19247	ScVO <sub>4</sub>	0.0000	2.64	Tier2	3.38	0.65	0.73

mp-19295	LuVO <sub>4</sub>	0.0341	2.60	Tier2	3.28	0.72	0.72
mp-19323	SmVO <sub>4</sub>	0.0000	3.00	Tier2	-	-	-
mp-19440	LiVO <sub>3</sub>	0.0000	2.82	Tier2	3.86	0.71	0.70
mp-19582	V <sub>2</sub> Zn <sub>3</sub> O <sub>8</sub>	0.0303	2.70	Tier2	4.21	0.70	0.65
mp-19707	V <sub>2</sub> Zn <sub>2</sub> O <sub>7</sub>	0.0000	2.55	Tier2	3.30	0.71	0.67
mp-25113	VInO <sub>4</sub>	0.0000	2.97	Tier2	3.96	0.61	0.71
mp-25140	GdVO <sub>4</sub>	0.0000	2.97	Tier2	3.77	0.68	0.71
mp-25142	V <sub>2</sub> Pb <sub>3</sub> O <sub>8</sub>	0.0032	2.98	Tier2	3.59	0.62	0.56
mp-25153	TiVO <sub>3</sub>	0.0000	2.97	Tier2	3.66	0.68	0.51
mp-25160	Na <sub>5</sub> VO <sub>5</sub>	0.0024	2.24	Tier2	2.91	0.69	0.58
mp-25559	MnVO <sub>4</sub>	0.0235	0.19	Tier2	0.35	0.09	0.29
mp-25796	V <sub>2</sub> Pb <sub>2</sub> O <sub>7</sub>	0.0000	2.87	Tier2	3.43	0.69	0.54
mp-32406	Ta <sub>9</sub> VO <sub>25</sub>	0.0000	2.61	Tier2	3.55	0.23	0.74
mp-32407	TaVO <sub>5</sub>	0.0000	2.17	Tier2	2.86	0.52	0.74
mp-32479	Tl <sub>3</sub> VO <sub>4</sub>	0.0000	2.60	Tier2	3.19	0.35	0.45
mp-32500	Mg <sub>2</sub> V <sub>2</sub> O <sub>7</sub>	0.0000	2.71	Tier2	3.65	0.72	0.71
mp-504820	VCl <sub>3</sub> O	0.0502	2.89	Tier2	3.55	0.66	0.08
mp-504923	V <sub>2</sub> Zn <sub>4</sub> O <sub>9</sub>	0.0186	2.55	Tier2	3.39	0.70	0.63
mp-505253	U <sub>2</sub> V <sub>2</sub> O <sub>11</sub>	0.0361	1.99	Tier2	3.34	0.33	0.55
mp-505265	La <sub>11</sub> V <sub>4</sub> O <sub>26</sub>	0.0066	1.02	Tier2	0.85	0.69	0.19
mp-505290	EuVO <sub>4</sub>	0.0000	2.78	Tier2	0.00	-	-
mp-505392	Ba <sub>3</sub> V <sub>4</sub> O <sub>13</sub>	0.0000	2.95	Tier2	3.70	0.70	0.69
mp-505679	HfV <sub>2</sub> O <sub>7</sub>	0.0000	2.65	Tier2	3.34	0.68	0.71
mp-541368	Tl <sub>4</sub> V <sub>2</sub> O <sub>7</sub>	0.0000	2.61	Tier2	2.94	0.63	0.34
mp-541501	VInO <sub>4</sub>	0.0205	2.86	Tier2	3.70	0.63	0.72
mp-559090	VBiO <sub>4</sub>	0.0209	2.53	Tier2	3.12	0.66	0.60
mp-559440	V <sub>2</sub> (CuO <sub>2</sub> ) <sub>5</sub>	0.0288	0.02	Tier2	1.17	0.12	0.48
mp-561207	UV <sub>2</sub> O <sub>8</sub>	0.0000	2.16	Tier2	3.10	0.16	0.69
mp-565447	ThV <sub>4</sub> O <sub>12</sub>	0.0000	2.57	Tier2	3.56	0.71	0.71
mp-565725	ZrV <sub>2</sub> O <sub>7</sub>	0.0000	2.59	Tier2	3.28	0.65	0.71
mp-572632	Mn <sub>2</sub> V <sub>2</sub> O <sub>7</sub>	0.0040	1.46	Tier2	1.12	0.66	0.26
mp-613172	VBiO <sub>4</sub>	0.0000	2.81	Tier2	3.23	0.69	0.57
mp-634381	V <sub>2</sub> Zn <sub>2</sub> O <sub>7</sub>	0.0306	2.02	Tier2	3.11	0.71	0.66
mp-647265	V <sub>2</sub> Bi <sub>7</sub> O <sub>15</sub>	0.0197	1.25	Tier2	-	-	-
mp-647385	V <sub>2</sub> Pb <sub>4</sub> O <sub>9</sub>	0.0000	2.91	Tier2	3.46	0.62	0.50
mp-690568	V <sub>2</sub> Bi <sub>4</sub> O <sub>11</sub>	0.0754	2.77	Tier2	3.37	0.61	0.59
mp-698685	V <sub>2</sub> Bi <sub>4</sub> O <sub>11</sub>	0.0518	2.30	Tier2	2.89	0.63	0.59

mp-763984	Na <sub>3</sub> VO <sub>3</sub>	0.0665	0.19	Tier2	0.00	-	-	
mp-766784	V <sub>3</sub> CoO <sub>8</sub>	0.0368	1.12	Tier2	0.89	0.73	0.18	
mp-769777	NbVO <sub>4</sub>	0.0805	1.35	Tier2	1.16	0.08	0.15	
mp-769888	Ho <sub>2</sub> V <sub>2</sub> O <sub>7</sub>	0.0771	0.51	Tier2	-	-	-	
mp-771386	VBO <sub>4</sub>	0.0681	2.63	Tier2	3.32	0.72	0.74	
mp-771484	VCoO <sub>4</sub>	0.0516	0.60	Tier2	1.07	0.13	0.54	
mp-771685	V <sub>4</sub> SnO <sub>12</sub>	0.0405	2.51	Tier2	3.37	0.70	0.71	
mp-771856	MnVO <sub>4</sub>	0.0763	0.50	Tier2	1.10	0.09	0.48	
mp-771872	V <sub>2</sub> NiO <sub>6</sub>	0.0000	2.69	Tier2	2.95	0.66	0.40	
mp-772238	V <sub>2</sub> SiO <sub>7</sub>	0.0522	2.44	Tier2	3.15	0.71	0.72	
mp-773218	V <sub>2</sub> FeO <sub>6</sub>	0.0247	1.72	Tier2	1.04	0.71	0.04	
mp-773430	NbV <sub>2</sub> O <sub>7</sub>	0.0669	0.00	Tier2	0.00	-	-	
mp-773455	V <sub>2</sub> SnO <sub>7</sub>	0.0000	2.61	Tier2	3.57	0.68	0.72	
mp-773503	V <sub>2</sub> CrO <sub>7</sub>	0.0347	0.62	Tier2	0.97	0.06	0.51	
mp-773930	V <sub>3</sub> (WO <sub>6</sub> ) <sub>2</sub>	0.0783	0.18	Tier2	0.00	-	-	
mp-774246	Nb <sub>9</sub> VO <sub>25</sub>	0.0015	2.00	Tier2	2.83	0.07	0.74	
mp-774376	Na <sub>5</sub> VO <sub>4</sub>	0.0560	0.81	Tier2	0.00	-	-	
mp-774963	Na <sub>5</sub> VO <sub>4</sub>	0.0766	0.31	Tier2	0.00	-	-	
mp-775001	V <sub>3</sub> FeO <sub>8</sub>	0.0802	1.26	Tier2	0.00	-	-	
mp-776985	MnV <sub>3</sub> O <sub>8</sub>	0.0573	1.08	Tier2	0.83	0.72	0.21	
mp-778022	Na <sub>3</sub> VO <sub>3</sub>	0.0652	0.40	Tier2	0.06	0.10	0.15	
mp-778222	Na <sub>3</sub> VO <sub>3</sub>	0.0730	0.59	Tier2	0.50	0.08	0.15	
mp-778356	Na <sub>8</sub> V <sub>2</sub> O <sub>7</sub>	0.0604	0.65	Tier2	0.00	-	-	
mp-778780	VBO <sub>4</sub>	0.0000	2.90	Tier2	3.61	0.72	0.73	
mp-780893	Na <sub>6</sub> V <sub>2</sub> O <sub>7</sub>	0.0756	0.91	Tier2	1.01	0.49	0.19	
mp-850239	Mn <sub>2</sub> V <sub>3</sub> O <sub>12</sub>	0.0770	0.00	Tier2	0.31	0.02	0.68	
mp-891955	Ca <sub>10</sub> V <sub>6</sub> O <sub>25</sub>	0.0288	2.32	Tier2	2.97	0.69	0.57	
mp-891956	Ca <sub>10</sub> V <sub>6</sub> O <sub>25</sub>	0.0000	2.35	Tier2	2.95	0.70	0.59	
mp-19096	Ba <sub>2</sub> VO <sub>4</sub>	0.0000	1.52	Tier3	1.72	0.68	0.20	-2.13
mp-554926	Sr <sub>2</sub> VO <sub>4</sub>	0.0396	1.53	Tier3	1.46	0.68	0.20	-4.30
mp-565780	Sr <sub>2</sub> VO <sub>4</sub>	0.0000	1.53	Tier3	1.45	0.72	0.21	-2.06
mp-566989	NpV <sub>4</sub> O <sub>12</sub>	0.0283	0.15	Tier3	2.06	0.46	0.09	--
mp-766869	V <sub>2</sub> Bi <sub>24</sub> O <sub>41</sub>	0.0068	1.66	Tier3	2.35	0.14	0.60	-4.56
mp-767265	V(Bi <sub>5</sub> O <sub>8</sub> ) <sub>5</sub>	0.0118	1.83	Tier3	2.47	0.18	0.59	-4.95
mp-849942	Na <sub>4</sub> VO <sub>4</sub>	0.0000	1.14	Tier3	1.31	0.27	0.20	-2.09
mp-853167	Na <sub>2</sub> VO <sub>3</sub>	0.0473	1.74	Tier3	1.92	0.73	0.15	-2.82
mp-18889	VAg <sub>3</sub> O <sub>4</sub>	0.0000	0.92	Tier7	1.70	0.19	0.34	-6.63

mp-18949	VFeO <sub>4</sub>	0.0146	1.82	Tier4	1.81	0.14	0.61	-5.78
mp-19412	VAg <sub>3</sub> O <sub>4</sub>	0.0301	0.60	Tier7	1.61	0.05	0.36	-7.64
mp-19418	VCrO <sub>4</sub>	0.0015	1.91	Tier7	2.21	0.44	0.28	-6.41
mp-19688	VCrO <sub>4</sub>	0.0127	2.21	Tier7	2.48	0.48	0.33	-6.82
mp-19692	Mn <sub>3</sub> V <sub>2</sub> O <sub>8</sub>	0.0000	1.92	Tier4	2.10	0.68	0.32	-6.17
mp-25122	VBiO <sub>4</sub>	0.0161	2.26	Tier4	2.71	0.67	0.61	-7.62
mp-504747	V <sub>2</sub> Cu <sub>3</sub> O <sub>8</sub>	0.0163	0.00	Tier7	1.73	0.18	0.51	-7.81
mp-504878	VBiO <sub>4</sub>	0.0161	2.30	Tier7	2.72	0.67	0.61	-7.58
mp-505456	V <sub>6</sub> Cu <sub>11</sub> O <sub>26</sub>	0.0292	0.00	Tier7	1.38	0.13	0.50	-7.41
mp-505508	V <sub>2</sub> Cu <sub>2</sub> O <sub>7</sub>	0.0064	0.00	Tier7	1.84	0.23	0.53	-8.04
mp-540630	VFeO <sub>4</sub>	0.0792	2.05	Tier7	2.10	0.17	0.55	-7.38
mp-540833	V <sub>2</sub> Co <sub>3</sub> O <sub>8</sub>	0.0000	1.74	Tier7	2.03	0.55	0.11	-6.27
mp-542151	V <sub>2</sub> Ni <sub>3</sub> O <sub>8</sub>	0.0000	2.57	Tier7	2.54	0.47	0.44	-7.39
mp-547693	V <sub>2</sub> Co <sub>2</sub> O <sub>7</sub>	0.0000	1.83	Tier6	2.00	0.63	0.13	-6.54
mp-557404	V <sub>2</sub> Ni <sub>2</sub> O <sub>7</sub>	0.0000	2.67	Tier7	2.72	0.54	0.38	-8.18
mp-559660	V <sub>2</sub> Cu <sub>2</sub> O <sub>7</sub>	0.0000	0.00	Tier7	1.84	0.27	0.52	-8.02
mp-565529	V <sub>4</sub> Fe <sub>2</sub> O <sub>13</sub>	0.0000	2.31	Tier4	2.54	0.19	0.66	-7.99
mp-600273	V <sub>2</sub> Cu <sub>3</sub> O <sub>8</sub>	0.0240	0.33	Tier4	1.47	0.24	0.53	-8.08
mp-614005	VCuO <sub>3</sub>	0.0770	0.80	Tier4	1.37	0.69	0.12	-7.18
mp-624691	VAgO <sub>3</sub>	0.0097	1.92	Tier4	2.65	0.70	0.25	-6.06
mp-687096	V <sub>2</sub> Cu <sub>2</sub> O <sub>7</sub>	0.0230	0.03	Tier4	1.85	0.22	0.52	-8.17
mp-761307	TiV <sub>2</sub> O <sub>7</sub>	0.0000	2.03	Tier4	2.73	0.50	0.72	-8.06
mp-763634	VCrO <sub>4</sub>	0.0606	1.83	Tier4	2.12	0.42	0.31	-6.52
mp-765013	Zr <sub>9</sub> VO <sub>20</sub>	0.0610	1.71	Tier4	1.96	0.73	0.21	-7.11
mp-766904	MnV <sub>4</sub> O <sub>12</sub>	0.0608	0.92	Tier4	1.81	0.28	0.70	-7.04
mp-767805	Zr <sub>11</sub> VO <sub>24</sub>	0.0517	1.77	Tier4	1.99	0.72	0.19	-6.90
mp-769887	NbVO <sub>5</sub>	0.0292	1.79	Tier4	2.45	0.50	0.74	-7.58
mp-769890	NbVO <sub>5</sub>	0.0000	1.89	Tier5	2.60	0.34	0.73	-9.12
mp-772351	NbVO <sub>5</sub>	0.0025	2.04	Tier4	2.76	0.36	0.73	-8.87
mp-773310	V <sub>2</sub> CoO <sub>6</sub>	0.0000	2.09	Tier7	2.16	0.67	0.08	-6.05
mp-777555	MnV <sub>2</sub> O <sub>6</sub>	0.0000	1.97	Tier4	2.18	0.71	0.24	-6.58
mp-850978	VFeO <sub>4</sub>	0.0715	1.92	Tier4	1.75	0.14	0.62	-7.60
mp-851269	V <sub>4</sub> Cr <sub>2</sub> O <sub>13</sub>	0.0000	2.33	Tier7	2.55	0.60	0.28	-7.40

## References

1. Fountaine KT, Lewerenz HJ, & Atwater HA (2016) Efficiency limits for photoelectrochemical water-splitting. *Nat Commun* 7:13706.
2. Khader MM, Saleh MM, & El-Naggar EM (1998) Photoelectrochemical characteristics of ferric tungstate. *Journal of Solid State Electrochemistry* 2(3):170-175.
3. Hardee KL & Bard AJ (1976) Semiconductor Electrodes: V. The Application of Chemically Vapor Deposited Iron Oxide Films to Photosensitized Electrolysis. *Journal of The Electrochemical Society* 123(7):1024-1026.
4. Mandal H, *et al.* (2016) Development of ternary iron vanadium oxide semiconductors for applications in photoelectrochemical water oxidation. *RSC Advances* 6(6):4992-4999.
5. Arai T, Konishi Y, Iwasaki Y, Sugihara H, & Sayama K (2007) High-throughput screening using porous photoelectrode for the development of visible-light-responsive semiconductors. *J Combinatorial Chem* 9(4):574-581.
6. Morton CD, Slipper IJ, Thomas MJK, & Alexander BD (2010) Synthesis and characterisation of Fe-V-O thin film photoanodes. *J Photochem Photobiol, A* 216(2-3):209-214.
7. Valenzuela MA, Bosch P, Jiménez-Becerrill J, Quiroz O, & Páez AI (2002) Preparation, characterization and photocatalytic activity of ZnO, Fe<sub>2</sub>O<sub>3</sub> and ZnFe<sub>2</sub>O<sub>4</sub>. *J Photochem Photobiol, A* 148(1-3):177-182.
8. De Haart LGJ & Blasse G (1985) Photoelectrochemical properties of ferrites with the spinel structure. *Solid State Ionics* 16:137-139.
9. Guo W, *et al.* (2015) Synthesis and Characterization of CuV<sub>2</sub>O<sub>6</sub> and Cu<sub>2</sub>V<sub>2</sub>O<sub>7</sub>: Two Photoanode Candidates for Photoelectrochemical Water Oxidation. *The J Phys Chem C* 119(49):27220-27227.
10. Seabold JA & Neale NR (2015) All 1st Row Transition Metal Oxide Photoanode for Water Splitting Based on Cu<sub>3</sub>V<sub>2</sub>O<sub>8</sub>. *Chem. Mater* 27(3):1005-1013.
11. Chen XY, *et al.* (2007) Application of weak ferromagnetic BiFeO<sub>3</sub> films as the photoelectrode material under visible-light irradiation. *Appl Phys Lett* 91(2):022114.
12. Jiang Z, *et al.* (2016) One-Pot Solvothermal Synthesis of Bi<sub>4</sub>V<sub>2</sub>O<sub>11</sub> as A New Solar Water Oxidation Photocatalyst. *Sci Rep* 6:22727.
13. Dang HX, Rettie AJE, & Mullins CB (2015) Visible-Light-Active NiV<sub>2</sub>O<sub>6</sub> Films for Photoelectrochemical Water Oxidation. *J Phys Chem C* 119(26):14524-14531.
14. Courtin E, *et al.* (2014) New Fe<sub>2</sub>TiO<sub>5</sub>-based nanoheterostructured mesoporous photoanodes with improved visible light photoresponses. *J Mater Chem A* 2(18):6567-6577.
15. Chemelewski WD, Mabayoje O, & Mullins CB (2015) SILAR Growth of Ag<sub>3</sub>VO<sub>4</sub> and Characterization for Photoelectrochemical Water Oxidation. *J Phys Chem C* 119(48):26803-26808.
16. Tang D, *et al.* (2015) Facile growth of porous Fe<sub>2</sub>V<sub>4</sub>O<sub>13</sub> films for photoelectrochemical water oxidation. *J Mater Chem A* 00:1-9.
17. Doumerc JP, Hejtmanek J, Chaminade JP, Pouchard M, & Krussanova M (1984) A photoelectrochemical study of CuWO<sub>4</sub> single crystals. *physica status solidi (a)* 82(1):285-294.
18. Sayama K, *et al.* (2003) Photoelectrochemical decomposition of water on nanocrystalline BiVO<sub>4</sub> film electrodes under visible light. *Chem Commun* (23):2908-2909.
19. Chan MKY & Ceder G (2010) Efficient Band Gap Prediction for Solids. *Phys Rev Lett* 105(19).
20. Gritsenko O, Vanleeuwen R, Vanlenthe E, & Baerends EJ (1995) Self-Consistent Approximation to the Kohn-Sham Exchange Potential. *Phys Rev A* 51(3):1944-1954.
21. Onida G, Reining L, & Rubio A (2002) Electronic excitations: density-functional versus many-body Green's-function approaches. *Rev Mod Phys* 74(2):601-659.
22. Hybertsen MS & Louie SG (1986) Electron correlation in semiconductors and insulators: Band gaps and quasiparticle energies. *Phys Rev B* 34(8):5390-5413.
23. Shih BC, Xue Y, Zhang PH, Cohen ML, & Louie SG (2010) Quasiparticle Band Gap of ZnO: High Accuracy from the Conventional G(0)W(0) Approach. *Phys Rev Lett* 105(14):146401.
24. Wen XD, Martin RL, Henderson TM, & Scuseria GE (2013) Density Functional Theory Studies of the Electronic Structure of Solid State Actinide Oxides. *Chem Rev* 113(2):1063-1096.
25. Kresse G & Furthmuller J (1996) Efficiency of ab-initio total energy calculations for metals and semiconductors using a plane-wave basis set. *Comp Mater Sci* 6(1):15-50.
26. Yan Q, *et al.* (2015) Mn<sub>2</sub>V<sub>2</sub>O<sub>7</sub>: An Earth Abundant Light Absorber for Solar Water Splitting. *Adv Energy Mater* 5(8):1401840.

27. Blochl PE (1994) Projector Augmented-Wave Method. *Phys Rev B* 50(24):17953-17979.
28. Perdew JP, Burke K, & Ernzerhof M (1996) Generalized gradient approximation made simple. *Phys Rev Lett* 77(18):3865-3868.
29. Heyd J, Scuseria GE, & Ernzerhof M (2003) Hybrid functionals based on a screened Coulomb potential. *J Chem Phys* 118(18):8207-8215.
30. Heyd J, Scuseria GE, & Ernzerhof M (2006) Hybrid functionals based on a screened Coulomb potential. *J Chem Phys* 124(21):219906.
31. Jain A, *et al.* (2011) A high-throughput infrastructure for density functional theory calculations. *Comp Mater Sci* 50(8):2295-2310.
32. Jain A, *et al.* (2011) Formation enthalpies by mixing GGA and GGA plus U calculations. *Phys Rev B* 84(4).
33. Ong SP, *et al.* (2013) Python Materials Genomics (pymatgen): A robust, open-source python library for materials analysis. *Comp Mater Sci* 68:314-319.
34. Castelli IE, *et al.* (2012) New cubic perovskites for one- and two-photon water splitting using the computational materials repository. *Energ Environ Sci* 5(10):9034-9043.
35. Castelli IE, *et al.* (2012) Computational screening of perovskite metal oxides for optimal solar light capture. *Energ Environ Sci* 5(2):5814-5819.
36. Stevanovic V, Lany S, Ginley DS, Tumas W, & Zunger A (2014) Assessing capability of semiconductors to split water using ionization potentials and electron affinities only. *Phys Chem Chem Phys* 16(8):3706-3714.
37. Scanlon DO, *et al.* (2013) Band alignment of rutile and anatase TiO<sub>2</sub>. *Nat Mater* 12(9):798-801.
38. Moses PG, Miao MS, Yan QM, & Van de Walle CG (2011) Hybrid functional investigations of band gaps and band alignments for AlN, GaN, InN, and InGaN. *J Chem Phys* 134( 8):084703.
39. Sun WH & Ceder G (2013) Efficient creation and convergence of surface slabs. *Surf Sci* 617:53-59.
40. Mitrovic S, *et al.* (2015) High-throughput on-the-fly scanning ultraviolet-visible dual-sphere spectrometer. *Rev Sci Instrum* 86:013904.
41. Zhou L, *et al.* (2015) High Throughput Discovery of Solar Fuels Photoanodes in the CuO–V<sub>2</sub>O<sub>5</sub> System. *Adv Energy Mater* 5:1500968.